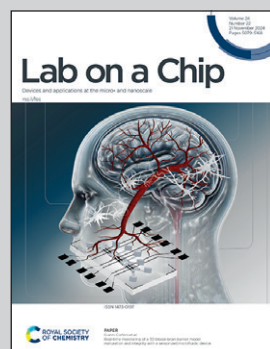


Showcasing research on Cost effective, rapid prototyping of 3D printing microwave sensors for microfluidic droplet monitoring from the Laboratory of Applied Microfluidics, Cardiff University, Wales, United Kingdom.

3D-printed microfluidic-microwave device for droplet network formation and characterisation

We present advancement in the field of microfluidic-microwave devices (MMDs), showcasing a novel 3D-printing approach to integrate liquid metal as an electrical conductor in the rapid prototyping of customized MMDs. This development opens new possibilities for sensitive, non-invasive characterization of low-volume liquids which is pivotal for applications in synthetic biology, biochemical research, and soft material studies. Image designed and illustrated by Adam Chard at *Croatoan Design*.

As featured in:



See Kai Silver *et al.*,
Lab Chip, 2024, **24**, 5101.



Cite this: *Lab Chip*, 2024, **24**, 5101

3D-printed microfluidic–microwave device for droplet network formation and characterisation†

Kai Silver, ^a Jin Li, ^a Adrian Porch, ^a William David Jamieson, ^b Oliver Castell, ^b Pantelitsa Dimitriou, ^a Colin Kallnik^a and David Barrow^a

Microfluidic–microwave devices (MMDs) have emerged as precision tools for the rapid, accurate, sensitive, and non-invasive characterisation of liquids in low-volumes. However, the fabrication of MMDs remains a significant challenge. This is due to the complexities associated with integrating fluidic ducts and electronic components. Herein, we present a versatile and economical 3D-printing approach using ducts filled with liquid metal as an electrical conductor. Cyclic olefin copolymer, polylactic acid, and polypropylene were identified as printable dielectric materials for MMD fabrication. Substrates of 3D-printed cyclic olefin copolymer exhibited the lowest loss tangent (0.002 at 2.7 GHz), making them suitable materials for high-frequency microwave devices. Liquid metal, specifically gallium-indium eutectic, was injected into the printed ducts to form electrically conductive microwave structures. Exemplary MMDs operating at 2 GHz integrated split-ring microwave resonators that serve as sensitive detection geometries able to measure changes in dielectric properties, with droplet-forming fluidic junctions and flow channels. The performance of 3D-printed MMDs for microwave droplet sensing was comprehensively evaluated. These devices were used in the formation and characterisation of water-in-oil emulsions, constructing definable lipid-segregated droplet interface bilayer (DIB) networks. This work indicates the feasibility of using 3D-printed manifolds for the rapid prototyping of customised MMDs, and also demonstrates the potential of MMDs as new analytical research tools in droplet-based materials and biochemistry studies.

Received 3rd May 2024,
Accepted 16th August 2024

DOI: 10.1039/d4lc00387j
rsc.li/loc

Introduction

Microfluidic–microwave devices (MMDs) represent a class of integrated instruments for processing and analysing liquid samples and soft matter.^{1–4} Droplet microfluidics has significantly advanced over the last three decades, bringing capabilities of precision liquid handling and high-throughput experimentation using droplet-based materials.^{5,6} Optical methods, such as fluorescence-based microscopy, can detect droplets 1 µm small, and operate at very high speeds, often at frequencies exceeding 10 kHz. However, the effectiveness of these methods can be compromised by factors like the transparency of the medium and the complexity of the optical setup.^{7,8} Meanwhile, microwave sensors have emerged as a technology for the rapid and sensitive characterisation of

materials, primarily by measuring their dielectric properties.^{9,10} The synergistic integration of microwave and microfluidic technologies enables highly accurate, non-invasive measurements of microfluidic flows, including droplets and emulsions.¹¹ If an MMD is capable of sensing *via* a low electric field interaction, the same MMD structure can be used as an actuator by ramping up the field (*i.e.* by increasing the microwave input power). Hence, MMDs can also enable the rapid dielectric heating of biological samples in an aqueous environment, including DNA plasmids and living cells.^{12,13} Recent developments in MMDs have extended their application to biosensing, notably in monitoring blood glucose levels,¹⁴ underpinning the potential of MMDs for innovations in analytical chemistry, biotechnology, pharmaceuticals development, and medical diagnostics.

The fabrication of MMDs can be technologically complex due to the intricate micromachining of fluidic and microwave structures within the same structure. Most MMDs are resonant structures, and it is crucial for device sensitivity that the microwave electric field energy is highly concentrated around the sample under test, in this case, the microfluidic duct. While a broad range of substrate materials can be used for constructing microfluidic devices (*e.g.* epoxy-glass laminates, polymers, silicon, glass, metals, and ceramics), for MMDs the

^a School of Engineering, Cardiff University, The Parade, Cardiff, CF24 3AA, UK.
E-mail: Lj40@cardiff.ac.uk

^b School of Pharmacy and Pharmaceutical Science, Cardiff University, King Edward VII Ave, Cardiff, CF10 3NB, UK

† Electronic supplementary information (ESI) available: Additional supporting information related to this study is available in the supplementary files accompanying this manuscript. Researchers interested in further exploring the data and methodologies are encouraged to contact the corresponding author, Jin Li or Kai Silver, for more details. See DOI: <https://doi.org/10.1039/d4lc00387j>



choice is much more restrictive due to the impact on microwave device performance; specifically, their low dielectric losses allow high *Q* (low loss) resonators to be formed. In a resonant MMD, a high quality (*Q*) factor leads to higher sensitivity for dielectric analysis; therefore, low microwave losses of the substrate material are imperative. Most MMDs are planar structures that enable the integration of microfluidic and microwave functionalities. High conductivity metals (*e.g.* copper or base metals coated with silver and gold) are often used to define the resonator structure, with ducts machined into substrates that feature low dielectric loss (*i.e.* low loss tangent). A convenient solution for MMDs is to use commercial, copper-clad, Teflon-based printed circuit boards¹⁵ which are available in a range of thicknesses (0.1 mm to few mm) and dielectric constants (2 to 10); all have very low microwave loss and low thermal coefficients, so that temporal temperature drifts are not an issue when sensing.

In recent years, 3D printing has been used for the fabrication of miniature devices,¹⁶ offering rapid prototyping of complex integrated structures. This manufacturing approach enables flexibility in device design and a rapid progression from a concept to prototype. Multiple materials, such as both dielectric and conductive filaments, can be 3D-printed on the same prototype, allowing for the fabrication of monolithic droplet-forming and sensing microfluidic devices with polymeric fluidic channels and integrated electrodes.^{17,18} Notably, liquid metals, such as gallium-indium eutectic, have been routinely used to form conductive parts in microfluidic devices.¹⁹ Liquid metal has also been injected into void channels to form irregular shaped, spiral electrodes within 3D-printed microchip electrophoresis devices.²⁰ 3D printing has also been used to form microwave structures, such as waveguides, resonators, and antennas,^{21–23} and some of them incorporate liquid metals to enable the real-time tuning of conducting parts.²⁴ Additionally, planar microwave resonators have been attached to 3D-printed microfluidic devices for the analysis of flowing liquids.²⁵ However, the use of liquid metals has not replaced conventional, costly, and complex manufacturing methods for the electrodes, and there has been no reports of utilizing liquid metal electrodes that comprise the entire conductive element. Therefore, the potential of 3D printing for MMD fabrication remains relatively unexplored to date, despite its promise for enhancing accessibility and customisability in various applications.

In this context, we introduce a simple fused filament fabrication (FFF) method for the 3D printing of MMDs, incorporating gallium-indium eutectic liquid metal. Various 3D-printable substrate materials and print settings were evaluated to optimise MMD performance. A comprehensive, step-by-step protocol is provided for the design and fabrication of MMDs by this approach. The demonstrated functional structures inside MMDs include split-ring microwave resonators, droplet-forming fluidic junctions, and droplet-handling fluidic circuits. The printed MMDs were used to generate and characterise single emulsions within flowing ducts. The performance of microwave droplet sensing

with the 3D-printed MMD was evaluated thoroughly. The microwave signatures resulting from the integration of the fluidic channel correlated with the formed droplet sizes, and were shown to be consistent with complementary optical measurements. Subsequently, the MMDs were used for the formation of lipid-segregated droplet interface bilayer (DIB) networks, and the number and the size of droplet components within a network were identified from the microwave readout. DIB networks have wide applications in molecular biology,^{26,27} artificial cellular membranes,²⁸ and the engineering of bottom-up synthetic cells and tissues.^{29,30} The presented 3D printing approach of MMDs is easily reproduced and has the potential to broaden MMD applications in miniaturised systems for potential bioengineering, biochemical and soft material research.

Experimental details

Materials

Ultimaker polylactic acid (PLA) and Ultimaker polypropylene (PP) filaments were purchased from CREATE Education Projects Ltd. Cyclic olefin copolymer (COC) filaments were purchased from CREAMELT. Plastic syringes (BD Plastipak) were purchased from Fisher Scientific. Microfluidic Teflon tubing (outer diameter 1.58 mm, inner diameter 0.80 mm), polyether ether ketone (PEEK) microfluidic fittings and connectors were purchased from Cole-Parmer UK. Gallium-indium eutectic and all chemicals used for droplet formation (phospholipid 1,2-diphytanoyl-sn-glycero-3-phosphocholine (DPhPC), hexadecane and silicone oil AR20) were purchased from Merck. A DPhPC-containing oil phase (60% hexadecane and 40% silicone oil AR20) was prepared at a concentration of 8 mg mL⁻¹, following an existing published protocol.³¹ SMA microwave connectors, conductive copper films and soldering wires were purchased from RS Components UK. All the materials were used as delivered unless otherwise mentioned.

Microwave–microfluidic device design and modelling

MMD structures were designed using the computer-aided design interface of COMSOL Multiphysics software. The geometry files built in COMSOL were exported as STL files for 3D printing. The electromagnetic fields within the MMDs were simulated using the RF module of COMSOL Multiphysics software (version 5.6). MATLAB 2023b, in conjunction with the signal processing toolbox, was used to post-process all numerical data.

Microwave–microfluidic device fabrication

The STL geometry files were sliced to G-Code files using Ultimaker CURA software (version 4.3.0). All printing profiles were used as the materials' default settings, unless otherwise specified, with the printing layer thickness set at 0.1 mm. The MMDs were fabricated using Ultimaker S5 Pro Bundle 3D printers, following the manufacturer's suggestions on the printing setup. The ambient humidity was regulated using a



domestic dehumidifier during 3D printing. The printed devices were stored alongside silica gel to avoid moisture formation. The assembly of MMDs is detailed in the Results section of this paper. Cyclic olefin copolymer (COC), polylactic acid and polypropylene were printed and tested as potential MMD substrate materials.

Microwave characterisation of MMD component materials and test liquids

To assess their suitability for MMD applications, the complex microwave permittivity of 3D-printed plastic sheets was first measured using a bespoke split-post dielectric resonator,³² operating at 2.7 GHz, and an Agilent E5071B Vector Network Analyser (VNA). Scattering parameter measurements (S_{21}) were made in the frequency domain to determine the resonant frequency and quality (Q) factor with and without a sample. Cavity perturbation analysis was then applied to extract the complex permittivity ϵ , whose real part (ϵ_1) is the dielectric constant (quantifying polarisation) and the imaginary part (ϵ_2) is the loss term. The samples were printed as 50 mm \times 30 mm \times 2 mm sheets. Both line and triangular printing formats were explored, with the infill percentage set to 100% (later adjusted to 50% for COC) and a Mitutoyo 103-129 micrometer was used to measure all sheet thicknesses.

Analogous complex microwave permittivity measurements of the various solvents used were performed using a cylindrical cavity resonator, operating in the TM_{010} mode at 2.4 GHz.³³ Liquids were held in a 1.5 mm inner diameter, 3 mm outer diameter clear FEP tube (FEP has a very low loss tangent of around 0.0002 at 2.4 GHz). The tube was placed along the axis of the cavity, where the microwave electric field was the highest and parallel to the tube. Cavity perturbation analysis was again used to calculate the complex permittivity values of all liquids, and these were used in the design and simulation of the MMDs.

Microfluidic experimental setup

Positive displacement syringe pumps (KD Scientific Legato 210) were used to inject fluids into the MMDs, using syringes, connectors, and tubing. The connections of tubing to MMDs were sealed with UV adhesive (Permabond) using a 365 nm UV torch. A photograph of the microwave-microfluidic experimental setup is shown in Fig. S1.† The input flow rate of fluids was controlled using the syringe pumps with actuation governed by a customised Python code to program droplet formation. Dispersed aqueous phases were injected into either T-shaped or flow-focusing droplet-forming junctions, with the aqueous phase broken into discrete droplets by a mineral oil continuous phase, and then flowed through the gap region of the split-ring microwave resonator designed within the 3D-printed MMDs.

Imaging, data collection and analysis

All photographs and videos were captured using a USB microscope (Dino-Lite, AM7915MZTL), or a high-speed

camera mounted (MEGA SPEED MS85KD4C1) on either a Nikon MM800 or a Nikon AZ100 optical measurement stereomicroscope. Either an Agilent E5071B VNA or an Agilent E5071C VNA was used for microwave measurements, controlled using a NI GPIB-USB-HS card and Python code utilising the PyVISA package. The size measurement of microfluidically formed droplets was analysed from acquired microscope images using ImageJ software. The data were processed with Microsoft Excel software before analysing using MATLAB 2021b with the signal processing toolbox 8.7 and curve fitting toolbox 3.6.

Results

Microwave-microfluidic device design

Fig. 1A and B present an example of a 3D-printed MMD incorporating a fluidic manifold with various channels and a liquid metal resonator for the purposes of water-in-oil single emulsion generation and microwave sensing. The substrate material was 3D-printed dielectric plastic blocks of COC. The split-ring resonator comprised a square-faced torus channel cavity filled with gallium-indium eutectic liquid metal (EGaIn) and was designed to achieve a fundamental resonant frequency of 2 GHz. This ring resonator had an inner radius of 7 mm, an outer radius of 8 mm, a height of 1 mm, and a gap width of 1.4 mm. Symmetrical input and output ports were formed using a pair of SMA connectors. The resonator was capacitively coupled *via* the electric field between the ring and the ends of the SMA connectors' centre pins, with the coupling strength adjusted by changing the spacing between the end of each pin and the ring. COMSOL Multiphysics was used to optimise the design of the ring resonator, in terms of the coupling strength and concentration of electric field energy in the ring's gap, which determines the sensitivity of the MMD and its signal-to-noise ratio (Fig. 1C and D). A vector network analyser (VNA) continuously measured the voltage reflection coefficient magnitude S_{21} in the frequency domain and the resonant frequency f_0 , quality factor (Q) and insertion loss L (*i.e.* the value of S_{21} at resonance, expressed in dB) from the VNA's trace markers whilst a microfluidic flow occurred within a duct that passed through the gap in the resonator's ring. The VNA's output power was 0 dBm (*i.e.* 1 mW); therefore, there was no measurable heating of the sample within the ring's gap at such low power levels.

The fluidic manifold included fluidic inlets, droplet-forming fluidic junctions (Fig. 1E), circuits, and outlets. An expansion duct directed the formed droplets and continuous carrier phase, to flow through the gap region of the split-ring resonator to enable the microwave sensing. In our 3D-printed MMDs, water retains a very high dielectric constant ϵ_1 of around 80 (ref. 34) at approximately 2.2 GHz, whereas the mineral oil phase or another oil phase, hexadecane, and air have much lower values of approximately 3.3, 2.0 and 1, respectively. Therefore, the water phase has a high induced electric dipole moment compared to oils and air. As a water



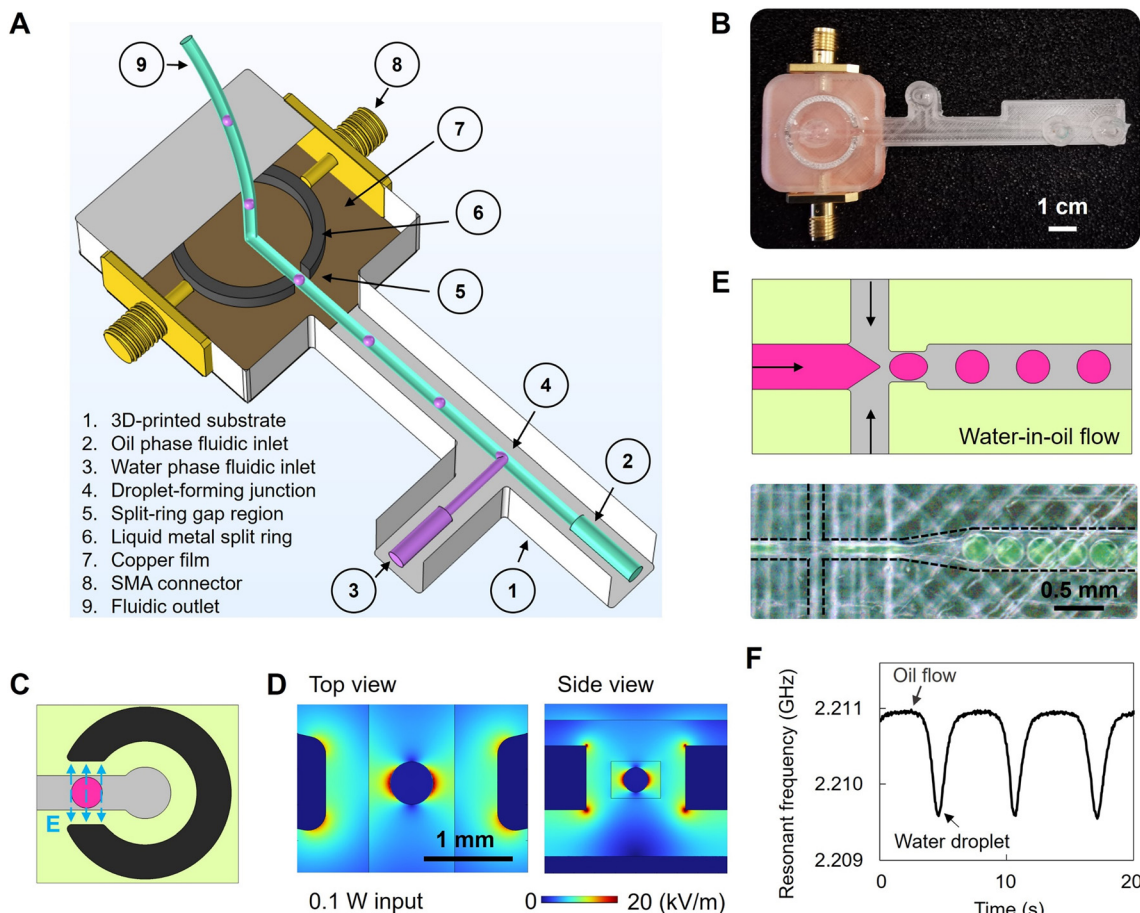


Fig. 1 3D-printed microwave–microfluidic device (MMD) for droplet formation and detection. **A**, Schematics of a 3D-printed MMD with labelled features. In this illustration, dispersed phase droplets are formed at a T-shaped droplet forming fluidic junction within a continuous phase fluid flow. The droplets pass though the gap region of a split-ring microwave resonator, created by liquid metal injection into 3D-printed ducts. The microwave resonator is activated by external microwave excitation through attached SMA connectors and grounded by a copper film which was adhered to the underside of the MMD. **B**, A sample of an assembled 3D-printed MMD. **C** and **D**, COMSOL simulation of the electric field at the gap region when a water droplet flows in the oil continuous phase. **E**, Droplet formation in a 3D-printed flow focusing droplet forming junction. **F**, An example of a microwave signature (based on continuous measurement of resonant frequency) when water droplets with a dispersed phase flow rate of 0.16 ml per hour was flowed through the gap region of the split-ring microwave resonator. The water and oil phases exhibit different dielectric properties, leading to different microwave resonant frequencies, represented as peaks and troughs in the trace.

droplet enters the gap region, more electrical energy is stored within the gap, causing f_0 to decrease. Additionally, due to the high dielectric loss associated with the dipole relaxation of water molecules, the quality factor (Q) decreases. The reductions in both f_0 and Q are less for oil than for water, so that the real-time monitoring of these changes provides real-time sensing of dispersed water droplets in a continuous, low-permittivity oil phase. An example of microwave signal detection is shown in Fig. 1F. When the gap region is filled with low-permittivity mineral oil, the resonant frequency is 2.211 GHz. When a water droplet entered the gap region, the resonant frequency reduced to 2.209 GHz, due to the greater stored energy (*i.e.* higher dielectric constant). Such MMD signatures of water droplets flowing in the oil phase are volumetric measurements and provide an approach to characterise liquid-based matrices and their morphology according to their dielectric properties and flow profiles

within the MMD's enclosed fluidic ducts without requiring optical access.

3D-printed MMD fabrication

A step-by-step guide for manufacturing the 3D-printed MMD is presented in Fig. 2. After fabricating the device substrate with a fused filament 3D printer, copper film tape was adhered to the bottom of the microwave structures to form a ground plane. The tape's thickness was 40 microns, which is above the normal thickness of 35 microns of a typical 305 g m^{-2} copper conductor on PCBs, and greater than the skin depth of copper at 2 GHz of 1.5 microns. Two SMA connectors were inserted into the sides of the microwave structure and the PTFE dielectric shielding of the SMA connector pin was removed, allowing the pin to be machined and positioned 1 mm away from the ring resonator. By



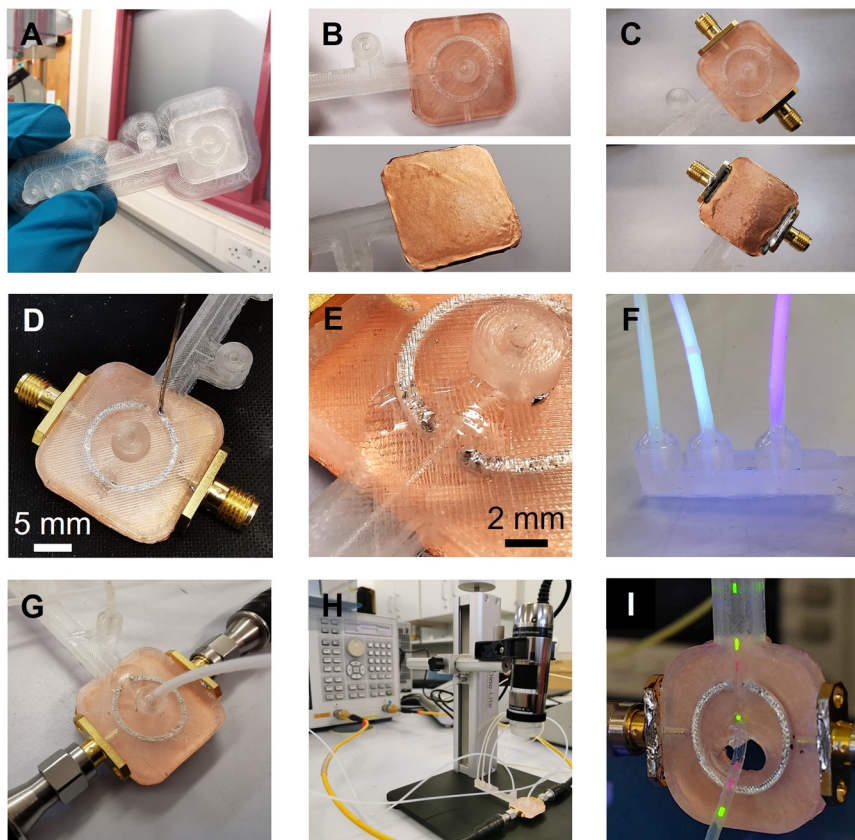


Fig. 2 Step-by-step guide for manufacturing, assembly, and operation of the 3D-printed MMD. **A**. The chassis of each MMD was fabricated using fused filament 3D printing. **B**. A conductive copper ground plate (adhesive foil) was then added below the planned position of the split-ring structure to reduce radiation losses and maintain a high *Q*-factor. **C**. Two SMA connectors were fixed in place and soldered to the ground plate. **D**. Liquid metal, gallium–indium eutectic (EGaIn), was injected to the void channel of the MMD chassis through open holes using a glass syringe and metal needle, forming the conductive split-ring structure as the microwave resonator. **E**. The open holes were sealed with UV adhesive and cured with a UV torch to prevent leakage of EGaIn and preserve the integrity of the microwave structure. **F**. The assembled MMD was connected to fluidic tubing (also sealed with UV adhesive) and syringe pumps. **G**. Flexible coaxial cables were used to connect the vector network analyser (VNA) to the MMD via its SMA connectors. **H**. A USB microscope was utilised to observe the droplet formation. The VNA was used to measure the magnitude of the scattering parameter S_{21} in real time and hence monitor the dispersed aqueous droplets and segments as they flowed through the EM field at the gap region of the split-ring resonator inside the MMD, shown in **I** in which water droplets with red and green dyes flowing through the SRR.

adjusting the pin's proximity to the resonator, without being in contact with the conductive part, the microwave coupling coefficient to the ring resonator could be altered. The SMA connectors, positioned 1 mm away from the ring, resulted in an insertion loss L of -9.1 dB at resonance, which was a good compromise to ensure a large enough signal to measure without the S_{21} becoming broadened or distorted due to excessively strong coupling. The ground contacts of the SMA connectors were soldered to the copper film. Liquid metal gallium–indium eutectic was then injected into the microwave structures through open holes in the substrate, forming the conductive paths. The open holes, fluidic inlets, and outlet connections were sealed with UV-curable adhesive to prevent leakage of the liquid metal and fluids. After assembly, the MMD was connected to a VNA machine for microwave signal transmission and sample measurements. For the droplet detection, fluids were injected into the MMD using syringes and syringe pumps, with fluidic tubing and

connectors. As the droplets passed through the gap (Fig. 2*I*) within the split-ring resonator, they were detected by the VNA and simultaneously imaged using an optical microscope.

The constructional substrate materials of the MMDs must have a suitably low microwave loss for appropriate microwave component performance. To assess the dielectric properties of 3D-printed substrates, plastic sheets were printed and measured to determine their complex permittivity ϵ , using a split-post dielectric resonator,³² as shown in Fig. S2.† Precise measurements were facilitated by aligning the electric field in the resonator's gap region parallel to the plastic sheet surfaces, so that measurements were insensitive to the gaps opened up between the sample and each puck of the dielectric resonator. The real ϵ_1 and imaginary ϵ_2 components of the complex permittivity were deduced using first order cavity perturbation analysis (eqn (1) and (2)), where $G = 2.20 \pm 0.01 \text{ m}^{-1}$ and is the resonator constant, derived from EM field COMSOL simulations, or, by measuring a known sample such as PTFE; t

is the plastic sheet thickness and the subscripts “s” and “0” are the measurements of resonant frequency f and quality factor Q , with and without sample, respectively.

$$\frac{\Delta f}{f_0} \equiv \frac{f_s - f_0}{f_0} \approx -G(\varepsilon_1 - 1)t \quad (1)$$

$$\Delta \left(\frac{1}{2Q} \right) \equiv \frac{1}{2Q_s} - \frac{1}{2Q_0} \approx G\varepsilon_2 t \quad (2)$$

Table S2† shows the complex permittivity of the various printed plastic sheets using different fabrication conditions. Measurement accuracy is primarily affected by the systematic error in sheet thickness ($\pm 50 \mu\text{m}$) and its uniformity. COC demonstrated superior dielectric properties amongst the tested materials, exhibiting low dielectric constant and low loss, which is crucial for high Q . Tests at different infills showed that lower infill COC is preferable for high-frequency systems in certain applications,^{35,36} despite the potential for increased leakage of microfluidic flows due to the air–plastic interfaces thus created.

COMSOL simulations (*e.g.* Fig. 1D) of the microwave electric field in the gap region of the split-ring resonator, where it is concentrated, has increased electric energy and polarization of the field (that induces dipole relaxation), causing a decrease in f_0 and Q as required for sensing. In the simulation, the ring's conductivity was set to that of EGaIn; the substrate was set to 100% infill COC, with the permittivity measured from the split-post method ($\varepsilon_1 = 5.35$ and $\varepsilon_2 = 0.01$, *i.e.* loss tangent = 0.002). The simulation results were consistent with the experimental microwave measurements. A broad sweep with a 1 GHz span about the split-ring resonance was used to generate S -parameters for the 2-port MMD. The simulated S_{21} data were then imported into a MATLAB program, where Lorentzian curve fitting was used to extract the resonant frequency and Q . The shape of microfluidic chambers and ducts through the split-ring gaps influenced the electric field. Under simulation, sharp corners of the ducts can enhance the peak electric field compared to rounded corners (as in Fig. 1D). The printing of the rounded and sharp corners is limited by the 20-micron precision of the 3D printer employed. Such fine features can become distorted when printed.

As shown in Fig. S3,† MMDs with identical designs were fabricated using different dielectric substrates. COC and PP offered good optical transparency, chemical resistance and low permeability of gas and liquid, making them suitable for various biomedical and microfluidic applications.³⁷ The 3D-printed PLA had a higher loss tangent but remained partially viable for microwave sensing. PLA is a common 3D-printing material and widely adopted in many 3D-printing applications.³⁸ Nylon prints were hydrophilic and have numerous applications in devices for life sciences and biomedicine, such as cell strainers, tubes, and dental dentures.³⁹ However, 3D-printed nylon has a relatively high microwave loss, making it unsuitable for MMDs, because of the resultant low Q factor and associated low sensitivity of a constructed device.

The MMDs demonstrated here are designed for analysing liquid samples within a microfluidic chamber. The chamber structure is a cube with an approximate volume of 6 μl , situated at the gap region of the optimised microwave split-ring resonator. Fig. S3E† depicts the S_{21} measurement of various samples in these MMDs, including air, an oil mixture, and deionised water (ddH₂O). All samples showed resonant frequency shifts when alternating between air, water, and oil mixtures in the COC, PP, and PLA MMDs. The oil mixture, comprising 40% silicone oil AR 20 and 60% hexadecane, is an oil phase commonly used in the formation of droplet interface bilayers (DIBs).⁴⁰ The central resonant frequencies (f_s) for water were approximately 2.1124 GHz, 2.27525 GHz, and 2.33545 GHz, for the PLA, COC and PP MMDs, respectively. This trend is consistent with the dielectric measurements of sheet materials using the split-post dielectric resonator, with the material of the highest dielectric constant giving the lowest resonant frequency for the same split-ring electrode geometry (since resonant frequency is proportional to $1/\sqrt{C}$, where C is the effective lumped-element capacitance of the structure, which is itself proportional to ε_1).

Injecting liquid metal into duct structures enables the patterning and incorporation of reconfigurable electrical elements, such as electrodes,⁴¹ sensors,⁴² antennas,⁴³ and interconnects.⁴⁴ In our fabrication approach for the MMD, gallium–indium eutectic (EGaIn) served as the conductive material, essential for transmitting microwaves. EGaIn's electrical conductivity is $3.6 \times 10^6 \text{ S m}^{-1}$ at room temperature, which is only one order of magnitude lower than that of noble metals,⁴⁵ and sufficient to realise a resonator with $Q > 100$. Also, at room temperature, its viscosity is $1.99 \times 10^{-3} \text{ Pa s}$ making it suitable for injection into circular micro-scale channels to form functional microwave components within the 3D-printed devices.

The effects of the liquid metal filling conditions within the 3D-printed channels on MMD sensing performance were assessed. The microwave skin effect δ in EGaIn (*i.e.* the effective depth to which surface currents flow) can be calculated using $\delta = 1/\sqrt{\pi\sigma\mu_0 f}$, which at 2 GHz for an electrical conductivity $\sigma = 3.6 \times 10^6 \text{ S m}^{-1}$ is around 6 μm . To create a thin EGaIn coating of the surface of the ring duct, a syringe with needles was employed to expel EGaIn carefully and slowly from the filled ring channel. Fig. S4† presents the cross section of the 3D-printed COC channels in various states: empty, fully filled, and with a skin of EGaIn. A residual layer of EGaIn, ranging in thickness from 10 μm to 100 μm , adhered to the channel walls, and was likely to be due to the rough surface microstructure created by the FFF 3D-printing process. The microwave sensing performance of the MMD before and after liquid metal removal was tested, as shown in Fig. S4D,† with air in the gap. The microwave structures resonated under both conditions, indicating effective microwave conduction along the thin EGaIn layer on the COC channel walls, thus forming a thin tube. A decrease in Q from 102 to 48 was noted, alongside a slight reduction in the central resonance frequency from 2.2212 GHz to 2.1756 GHz after liquid metal removal and is proposed to be



attributed to the increased current density in the narrow EGaIn layer, which then increases its effective resistance (and $Q \propto 1/R$). Consequently, the air-assisted EGaIn removal had a minimal effect on the resonator sensing performance, except for a small reduction in measurement resolution due to the decreased Q -factor. Additionally, complete removal of EGaIn from the 3D-printed MMDs was achieved by flushing with a 1 M NaOH solution through the ring structures, which resulted in the disappearance of the MMD resonance after complete liquid metal removal.

3D-printed MMD performance on droplet formation and sensing

3D-printed microfluidics have been designed to generate complex emulsion droplets.^{46,47} The addition of microwave

functionality to create MMDs can be used for aqueous droplet formation and processing for non-invasive, volumetric analysis of flowing droplet materials in real-time. As shown in Fig. 3, microfluidically formed droplets flowed in the printed channel through the gap region of the microwave split ring resonator. An additional fluidic inlet injected an oil phase to control the distance between adjacent droplets and their linear speed of travel through the channel, ensuring that each droplet passed through the gap region of the split-ring resonator without interference from adjacent droplets. Fig. 3B shows that when the droplet phase inflow rate is increased, the droplets are formed faster, as detected from the microwave sensing readout. The microwave sensing is provided by the scanning of the resonant frequency of the liquid materials within the split ring region at up to 1.5 MHz over the bandwidth (e.g. 30 MHz span) set

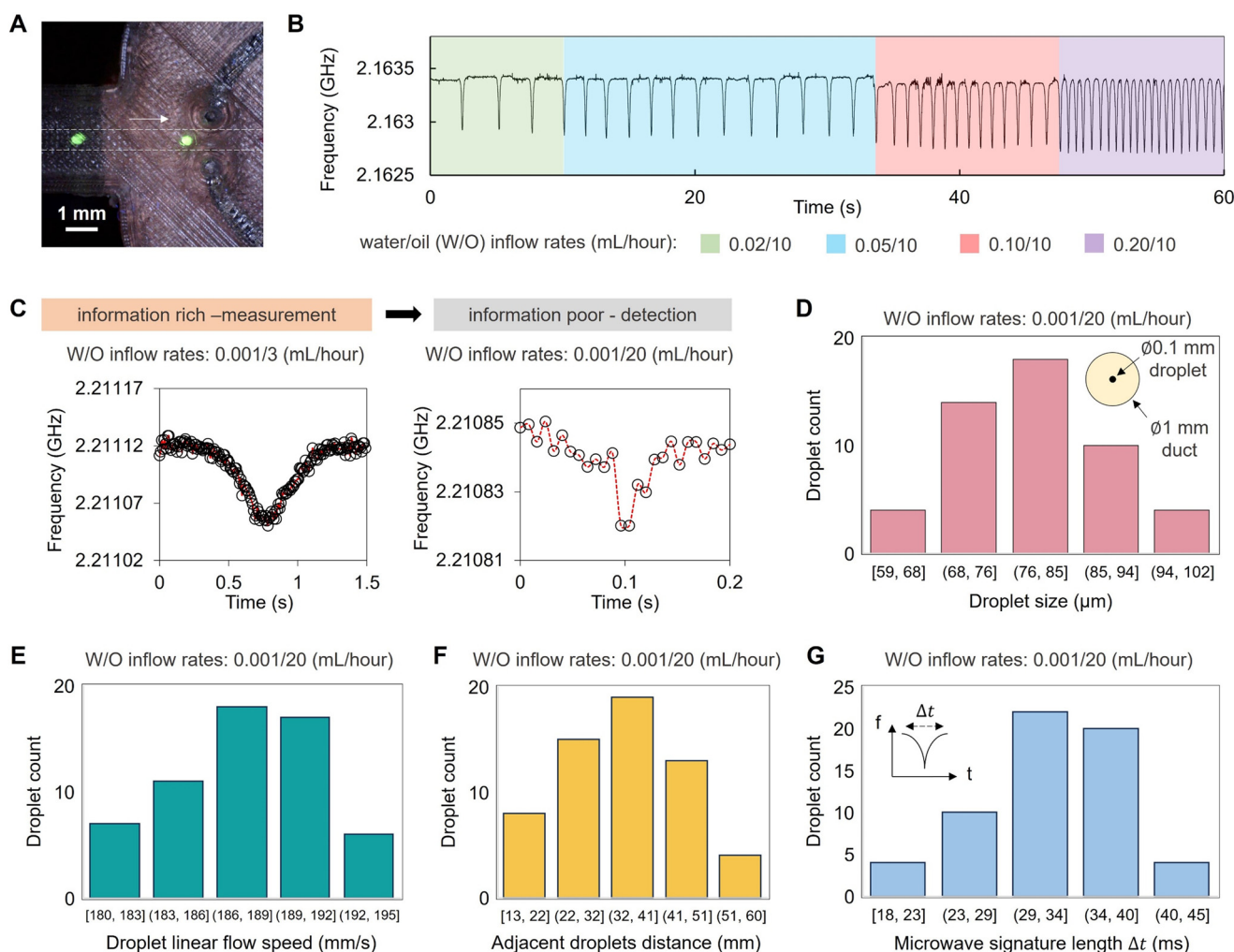


Fig. 3 Performance of the 3D-printed MMD on droplet sensing. A. Neighbouring droplets flowing through the split ring resonator. B. Microwave sensing readout of water droplets flowing in the continuous oil phase at different inflow rates. C. Acquired data points of individual droplets at different inflow rates. The quantity of data points determines either volumetric measurement (information rich) or detection (information poor) of the water droplet in the oil flow using the microwave sensing. D. The size of the smallest water droplets, which can be formed and detected in our 3D-printed MMD experiment setup, is around 60 μm flowing in a 1 mm wide fluidic duct. The linear flow velocity of these droplets is approximately 190 mm s^{-1} (E), and the distance between adjacent droplets is approximately 35 mm (F), measured with a high-speed camera. It took approximately 35 ms for the droplet to flow across the microwave sensing region (G).

on the VNA, with the channel contents in the split-ring gap impacting the measured resonance. The microwave scanning rate is sufficient for the droplet detection under flow conditions in our case, and the readout is constrained by the data processing speed of the CPU of the computing terminal. With a typical laptop workstation (e.g. Dell Latitude 5440), data points can be collected every 0.006 s. Fig. 3C shows examples of the microwave sensing readout of water droplets flowing through the split ring resonator under different oil continuous phase inflow rates. When the oil phase inflow rate was lower, the droplet spent a longer time at the gap region and more data points were derived for the measurements of droplet size and speed. Meanwhile, when the oil inflow rate was higher and the droplet transit speed was faster, the data points acquired for each droplet were fewer in number such that in our acquisition regime at faster flow rates; our MMD reports droplet detection with insufficient measurement time for volumetric characterisation. In this regime, we find that the smallest droplets that can be formed and detected in our 3D-printed MMD are around 60 μm , flowing in a 1 mm wide duct (Fig. 3D), which were confirmed optically using a high-speed camera at 1300 fps. These water droplets in oil were formed with the water/oil inflow rates of 0.001/20 mL per hour,

providing a linear flow speed of around 190 mm s^{-1} (Fig. 3E) with approximately 35 mm distance between the adjacent droplets (Fig. 3F), presenting the upper limit of the droplet speed detection in our experimental setup (Fig. 3G).

With sufficient data points (Fig. 3C, left), droplet sizes can be analysed from the microwave data of droplet flows, since the microwave sensing readout (either a shift in resonant frequency or a change in loss) is proportional to the sample volume, assuming that the droplet and continuous phases have constant dielectric properties. In our work, droplet sizes were modulated by the input flow rates, as shown in Fig. 4, and the polydispersity of droplets was calculated. Microwave sensing readouts were used to determine the droplet size and polydispersity simultaneously. As shown in Fig. 4A, smaller droplets resulted in a reduction of the measured frequency change. The average decrease in resonant frequency for 0.7 mm diameter droplets was \sim 1 MHz, representing a 50 \times greater decrease than the background variation. Fig. 4B shows the size distribution of microfluidically formed droplets under different inflow rates, for which the droplet sizes were measured optically. The microwave sensing of the droplets shown in Fig. 4B exhibits high sensitivity to their volume variations, enabling the measurement of the uniformity of the microfluidically-formed droplets using

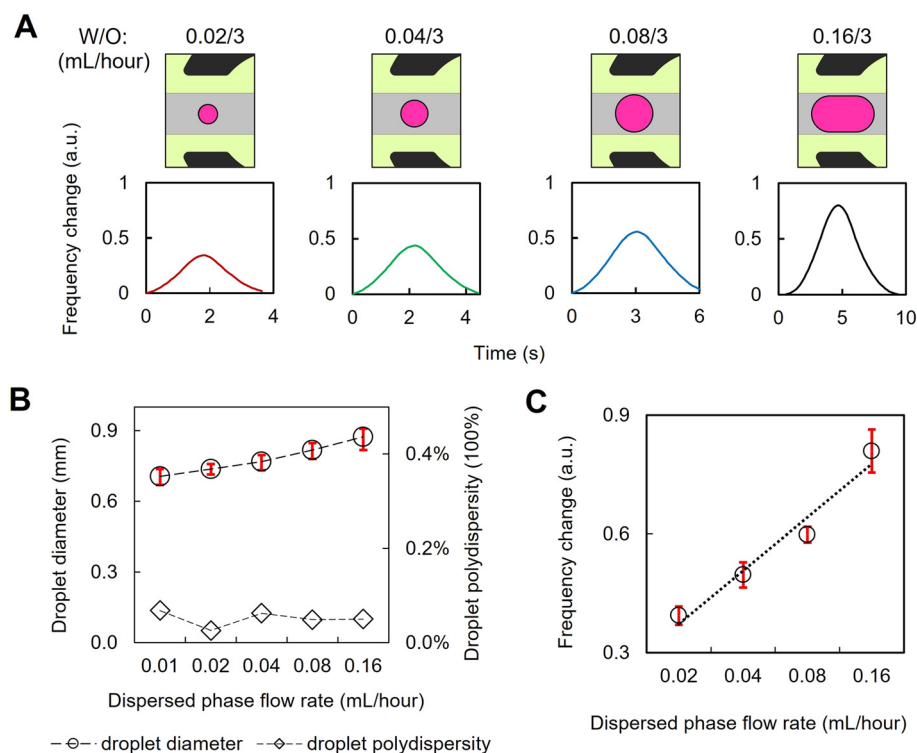


Fig. 4 Droplet size characterisation using microwave sensing readouts. A. Different sizes of water droplets were formed in the oil flow controlled by inflow rate combinations. Normalised microwave readout frequency change for droplets of different sizes corresponding to the input flow rates. B. Size distribution and polydispersity of droplets at varying flow rates, measured with an optical microscope. The continuous phase flow was maintained at 0.1 mL per hour for all sample groups, with $N = 30$ for each data point. Error bars indicate the maximum and minimum droplet sizes within the sample groups with polydispersity = $(\text{mean diameter})^2/(\text{standard deviation})^2$. C. Relationship between droplet diameter and normalised frequencies. Error bars represent frequency variation with $N = 30$ for each data point.

microwave readout data as presented in Fig. 4C. After the calibration of the microwave readouts against the optical measurement, this technique can characterise droplet populations of water-in-oil emulsions with diverse components and encapsulants. Such an approach offers an accurate, non-invasive method to analyse complex emulsions *in situ*, which is potentially beneficial for non-transparent microfluidic substrates, like the PLA device shown in Fig. S3,[†] or for liquid samples that are non-light transmissive or require protection from light exposure. The MMD generates

real-time droplet size distribution data for entire droplet populations, eliminating the need for post-sampling droplet collection and optical measurement with manual operations.

3D-printed MMD for lipid-coated droplet network formation and characterisation

The droplet-forming and sensing abilities of the MMDs were further demonstrated for the construction of lipid-segregated droplet interface bilayer (DIB) networks. These droplet

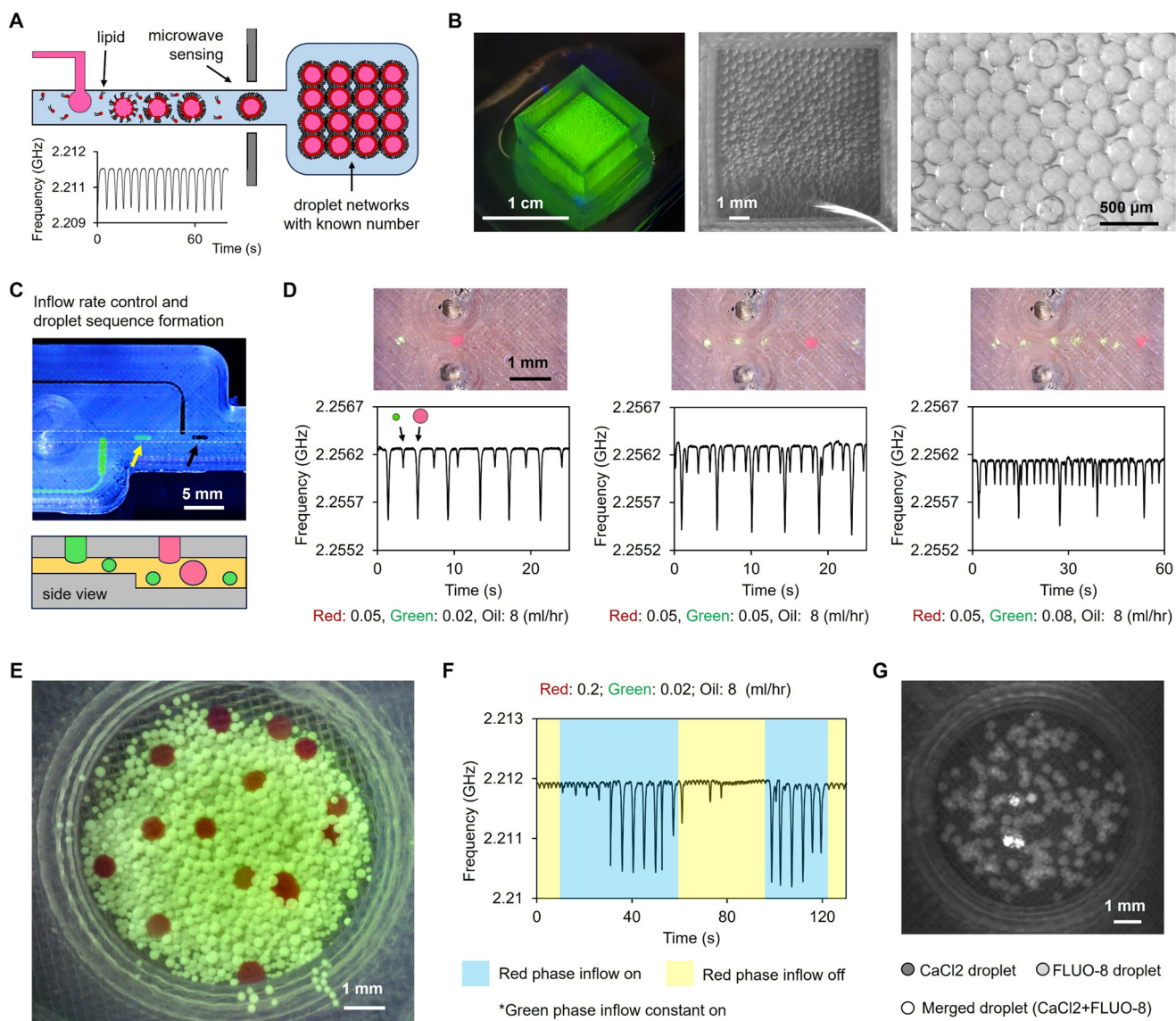


Fig. 5 Droplet network formation and characterisation using 3D-printed MMDs. **A.** Formation of lipid-coated water droplets in a continuous oil phase flow inside a microfluidic duct with microwave sensing, leading to uniform droplet interface bilayer (DIB) network formation when collected in an oil-phase prefilled dish (**B**). **C.** Droplet generation at 3D-printed, T-shaped, droplet-forming fluidic junctions. **D.** Droplet sequences were formed at different inflow rate combinations. The microwave sensing readout registered the droplet sizes and positions in the flow. **E.** DIB networks composed of two types of droplets that the large red droplets were formed with on/off control of the inflow, which were recorded in the microwave sensing readout (**F**). **G.** DIB networks composed of CaCl_2 buffer droplets (dark, cannot be seen here), FLUO-8 droplets (grey), and their merged droplets (bright). FLUO-8 is a calcium ion sensitive dye that becomes fluorescent when binding with calcium ions. The DIBs were formed in the same approach as shown in Fig. 5C and D, and the merge of droplets possibly happened during the droplet collection. These figures show that the DIB construction is relative stable with a low droplet coalescence rate using the 3D-printed MMDs to both control the droplet formation and characterisation.



networks gain functionality through the artificial cellular membranes and reagents encapsulated within each droplet component, for example for cell-free expression and synthesis.⁴⁸ In our study, DPhPC lipid was dispersed in the oil phase. After forming aqueous droplets in the duct, lipids self-assembled at the water–oil interface, forming a lipid monolayer around the aqueous droplets. Upon contact of two lipid monolayer coated droplets, a lipid bilayer is formed, comparable in structure to the cell membrane. The aqueous droplets were then collected in a 3D-printed COC Petri dish, where the droplets aggregated and interconnected to form tissue-like DIB networks, as shown in Fig. 5A and B and S5.† Droplets were formed from different aqueous phases at multiple droplet forming junctions within the MMDs, and the droplet size was controlled by the fluidic structures and the inflow rates (Fig. 5C). Sequences of droplets were formed in the fluidic duct with the droplet size and position registered in the microwave readout. W-shaped signatures were observed (Fig. S6†) if the adjacent droplets were closed when passing by the split-ring region. Fig. 5E and F show that a specific type of droplet can be formed at a certain time point by the on/off control of their inflow during the droplet network formation. Coalescence of minor droplets was observed, which possibly happened at the interface of the MMD and the outlet tubing. As demonstrated in Fig. 5G, CaCl_2 buffer droplets and FLUO-8 (Ca^{2+} sensitive dye) containing KCl buffer droplets were generated and collected in a dish. Only few droplets lit up due to the merging of CaCl_2 and FLUO-8 droplets, showing a stable microfluidic approach of droplet generation and transportation. Hence, the approximate number of droplets was deduced from the microwave readout by calculating the peak values in the traces, allowing the MMD to serve as a non-invasive counting tool for droplet network formation (Fig. S7†). This method could be employed to provide real-time droplet information for DIB network fabrication or bio-printing applications, allowing analysis and precise time reporting of individual droplets as they are made and deposited, thus providing potentially valuable real-time information for quality control, or feedback into bioprinting spatial manipulations, aiding in depositing the right droplets, in the right place, at the right time.

Discussion

We have presented a comprehensive study of using a fused filament 3D printing method to fabricate microfluidic–microwave devices, incorporating microwave split-ring resonators fabricated *via* liquid metal injection into printed ducts. We detailed the device designs, printing material selections, and the fabrication and assembly processes. The microwave sensing performance of 3D-printed COC MMDs on water-in-oil emulsions was evaluated, yielding results comparable to conventional metal-machined resonators.⁴⁹ We demonstrated the application of MMDs for reagent and droplet morphology detection in a flow. These findings demonstrate the efficacy, versatility, and robustness of this

fabrication approach for constructing customised microfluidic–microwave devices that can be used for the formation and non-invasive characterisation of single emulsions.

Most importantly, 3D printing introduces the capability to organise functional fluidic circuits and customised electrical elements on the same substrate. This represents a promising engineering tool for soft matter development and the construction of bottom-up synthetic cells and tissues with enhanced function. We showcased the use of 3D-printed MMDs in determining the compositions of microfluidically formed DIB networks. Future work will integrate this experimental setup with precision droplet deposition methods to analyse *in situ* droplet distributions and network configurations, enabling studies of networked chemical reactions in macroscale artificial cellular systems.

Although the performance of 3D-printed MMDs is currently constrained by the limits in resolution of the fused filament 3D printers used here, more accurate and high-resolution 3D printing platforms, along with more bespoke dielectric materials for microwave and high-frequency engineering, are available.^{50–52} The methodology shown here is generally applicable to emerging 3D printing approaches and other substrate and dielectric materials and thus can be expected to be significantly improved with these advanced tools to produce customised MMDs and other microelectrode-embedded microfluidic devices featuring complex microstructures.

Data availability

The data that support the findings of this study are available from the corresponding author upon reasonable request. The datasets generated and/or analysed in the current study are available from the author upon reasonable request.

Conflicts of interest

There are no conflicts to declare.

Acknowledgements

JL, DB and AP conceived the original idea. JL led the research, with support from KS, DB and AP. KS, JL, WDJ, OC, CK, and PD performed the experiments. JL and KS wrote the manuscript, with revisions by DB, AP and OC. This work was partially supported by the European Horizon 2020 project ACDC (Artificial Cells with Distributed Cores) under project award number 824060 and the European Union Horizon Europe EIC 2023 Pathfinder Open programme BioHhOST (bio-hybrid hierarchical organoid-synthetic tissue) under grant agreement No 101130747. The authors also would like to thank Cardiff School of Engineering for the financial support on consumables used in this work. The authors would like to thank Jacob Fielder, Ilyas Rasool, Daniel Sweeney, Samuel Bastow, Chanelle Nagra and Jake Richardson for their preliminary work on device fabrication.



References

- 1 M. H. Zarifi, H. Sadabadi, S. H. Hejazi, M. Daneshmand and A. Sanati-Nezhad, Noncontact and Nonintrusive Microwave-Microfluidic Flow Sensor for Energy and Biomedical Engineering, *Sci. Rep.*, 2018, **8**, 139.
- 2 M. Baghelani, Z. Abbasi, M. Daneshmand and P. E. Light, Non-invasive continuous-time glucose monitoring system using a chipless printable sensor based on split ring microwave resonators, *Sci. Rep.*, 2020, **10**, 12980.
- 3 B. Camli, *et al.*, Rapid prototyping of noncontact microwave microfluidic devices for sensing applications, *J. Micromech. Microeng.*, 2021, **31**, 097001.
- 4 O. Peytral-Rieu, D. Dubuc and K. Grenier, Microwave-Based Sensor for the Noninvasive and Real-Time Analysis of 3-D Biological Microtissues, Microfluidic Improvement and Sensitivity Study, *IEEE Trans Microwave Theory Techn.*, 2023, **71**, 4996–5003.
- 5 L. Zhang, *et al.*, High-throughput microfluidic droplets in biomolecular analytical system: A review, *Biosens. Bioelectron.*, 2023, **228**, 115213.
- 6 T. Moragues, *et al.*, Droplet-based microfluidics, *Nat. Rev. Methods Primers*, 2023, **3**, 1–22.
- 7 J. Wu, G. Zheng and L. M. Lee, Optical imaging techniques in microfluidics and their applications, *Lab Chip*, 2012, **12**, 3566–3575.
- 8 S. Hengoju, O. Shvydkiv, M. Tovar, M. Roth and M. A. Rosenbaum, Advantages of optical fibers for facile and enhanced detection in droplet microfluidics, *Biosens. Bioelectron.*, 2022, **200**, 113910.
- 9 M. S. Venkatesh and G. S. V. Raghavan, An overview of dielectric properties measuring techniques, *Can. Biosyst. Eng.*, 2005, **47**, 15–30.
- 10 K. Li, *et al.*, Microwave dielectric properties and thermochemical characteristics of the mixtures of walnut shell and manganese ore, *Bioresour. Technol.*, 2019, **286**, 121381.
- 11 Y. Yan, *et al.*, Rapid, non-invasive characterization of the dispersity of emulsions *via* microwaves, *Chem. Sci.*, 2018, **9**, 6975–6980.
- 12 D. J. Marchiarullo, *et al.*, Low-power microwave-mediated heating for microchip-based PCR, *Lab Chip*, 2013, **13**, 3417–3425.
- 13 J. Gao, *et al.*, Nanotube Assisted Microwave Electroporation for Single Cell Pathogen Identification and Antimicrobial Susceptibility Testing, *Nanomedicine*, 2019, **17**, 246–253.
- 14 M. Zhang, *et al.*, Microfluidic microwave biosensor based on biomimetic materials for the quantitative detection of glucose, *Sci. Rep.*, 2022, **12**, 15961.
- 15 L. Jasińska and K. Malecha, Microfluidic Modules Integrated with Microwave Components—Overview of Applications from the Perspective of Different Manufacturing Technologies, *Sensors*, 2021, **21**, 1710.
- 16 K. Malecha, *et al.*, Monolithic Microwave-Microfluidic Sensors Made with Low Temperature Co-Fired Ceramic (LTCC) Technology, *Sensors*, 2019, **19**, 577.
- 17 R. D. Sochol, *et al.*, 3D printed microfluidics and microelectronics, *Microelectron. Eng.*, 2018, **189**, 52–68.
- 18 L. C. Duarte, C. L. S. Chagas, L. E. B. Ribeiro and W. K. T. Coltro, 3D printing of microfluidic devices with embedded sensing electrodes for generating and measuring the size of microdroplets based on contactless conductivity detection, *Sens. Actuators, B*, 2017, **251**, 427–432.
- 19 R. F. Quero, B. M. D. C. Costa, J. A. F. da Silva and D. P. de Jesus, Using multi-material fused deposition modeling (FDM) for one-step 3D printing of microfluidic capillary electrophoresis with integrated electrodes for capacitively coupled contactless conductivity detection, *Sens. Actuators, B*, 2022, **365**, 131959.
- 20 K. Khoshmanesh, *et al.*, Liquid metal enabled microfluidics, *Lab Chip*, 2017, **17**, 974–993.
- 21 B. M. C. Costa, *et al.*, 3D-printed microchip electrophoresis device containing spiral electrodes for integrated capacitively coupled contactless conductivity detection, *Anal. Bioanal. Chem.*, 2022, **414**, 545–550.
- 22 A. Salim, S. Ghosh and S. Lim, Low-Cost and Lightweight 3D-Printed Split-Ring Resonator for Chemical Sensing Applications, *Sensors*, 2018, **18**, 3049.
- 23 T. A. Elwi, Printed Microwave Metamaterial-Antenna Circuitries on Nickel Oxide Polymerized Palm Fiber Substrates, *Sci. Rep.*, 2019, **9**, 2174.
- 24 A. M. Mohammed, Y. Wang and M. J. Lancaster, 3D printed coaxial microwave resonator sensor for dielectric measurements of liquid, *Microw. Opt. Technol. Lett.*, 2021, **63**, 805–810.
- 25 B. D. Wiltshire, M. A. Rafi and M. H. Zarifi, Microwave resonator array with liquid metal selection for narrow band material sensing, *Sci. Rep.*, 2021, **11**, 8598.
- 26 B. D. Wiltshire and M. H. Zarifi, 3-D Printing Microfluidic Channels With Embedded Planar Microwave Resonators for RFID and Liquid Detection, *IEEE Microw. Wirel. Compon. Lett.*, 2019, **29**, 65–67.
- 27 L.-Q. Gu and J. Wook Shim, Single molecule sensing by nanopores and nanopore devices, *Analyst*, 2010, **135**, 441–451.
- 28 M. Allen-Benton, H. E. Findlay and P. J. Booth, Probing membrane protein properties using droplet interface bilayers, *Exp. Biol. Med.*, 2019, **244**, 709–720.
- 29 S. Lee and H. Bayley, Reconstruction of the Gram-Negative Bacterial Outer-Membrane Bilayer, *Small*, 2022, **18**, 2200007.
- 30 A. D. Graham, *et al.*, High-Resolution Patterned Cellular Constructs by Droplet-Based 3D Printing, *Sci. Rep.*, 2017, **7**, 7004.
- 31 A. Alcinesio, *et al.*, Controlled packing and single-droplet resolution of 3D-printed functional synthetic tissues, *Nat. Commun.*, 2020, **11**, 2105.
- 32 J. Li, *et al.*, Building programmable multicompartment artificial cells incorporating remotely activated protein channels using microfluidics and acoustic levitation, *Nat. Commun.*, 2022, **13**, 4125.
- 33 J. Krupka, *et al.*, Uncertainty of complex permittivity measurements by split-post dielectric resonator technique, *J. Eur. Ceram. Soc.*, 2001, **21**, 2673–2676.



34 J. A. Cuenca, E. Thomas, S. Mandal, O. Williams and A. Porch, Investigating the Broadband Microwave Absorption of Nanodiamond Impurities, *IEEE Trans. Microwave Theory Tech.*, 2015, **63**, 4110–4118.

35 U. Kaatze, Complex permittivity of water as a function of frequency and temperature, *J. Chem. Eng. Data*, 1989, **34**, 371–374.

36 S. Dev and R. Srivastava, Effect of infill parameters on material sustainability and mechanical properties in fused deposition modelling process: a case study, *Prog. Addit. Manuf.*, 2021, **6**, 631–642.

37 K. Saeed, *et al.*, Planar Microwave Sensors for Complex Permittivity Characterization of Materials and Their Applications. In: *Applied Measurement Systems*, IntechOpen, 2012, DOI: [10.5772/36302](https://doi.org/10.5772/36302).

38 A. Agha, *et al.*, A Review of Cyclic Olefin Copolymer Applications in Microfluidics and Microdevices, *Macromol. Mater. Eng.*, 2022, **307**, 2200053.

39 T. M. Joseph, *et al.*, 3D printing of polylactic acid: recent advances and opportunities, *Int. J. Adv. Manuf. Tech.*, 2023, **125**, 1015–1035.

40 M. Shakiba, *et al.*, Nylon—A material introduction and overview for biomedical applications, *Polym. Adv. Technol.*, 2021, **32**, 3368–3383.

41 M. M. Makhoul-Mansour and E. C. Freeman, Droplet-Based Membranous Soft Materials, *Langmuir*, 2021, **37**, 3231–3247.

42 J.-H. So and M. D. Dickey, Inherently aligned microfluidic electrodes composed of liquid metal, *Lab Chip*, 2011, **11**, 905–911.

43 H. Ota, *et al.*, Highly deformable liquid-state heterojunction sensors, *Nat. Commun.*, 2014, **5**, 5032.

44 K. N. Paracha, A. D. Butt, A. S. Alghamdi, S. A. Babale and P. J. Soh, Liquid Metal Antennas: Materials, Fabrication and Applications, *Sensors*, 2020, **20**, 177.

45 M. Li, *et al.*, Liquid metal-based electrical interconnects and interfaces with excellent stability and reliability for flexible electronics, *Nanoscale*, 2019, **11**, 5441–5449.

46 C. Dodd, The Electrical Resistance of Liquid Gallium in the Neighbourhood of its Melting Point, *Proc. Phys. Soc., London, Sect. B*, 1950, **63**, 662.

47 Q. Ji, *et al.*, A Modular Microfluidic Device *via* Multimaterial 3D Printing for Emulsion Generation, *Sci. Rep.*, 2018, **8**, 4791.

48 J. Li, *et al.*, Formation of Polarized Functional Artificial Cells from Compartmentalized Droplet Networks and Nanomaterials Using One-Step Dual-Material 3D-Printed Microfluidics, *Adv. Sci.*, 2020, **7**, 1901719.

49 M. J. Booth, I. Cazimoglu and H. Bayley, Controlled deprotection and release of a small molecule from a compartmented synthetic tissue module, *Commun. Chem.*, 2019, **2**, 142.

50 A. A. Abduljabar, D. J. Rowe, A. Porch and D. A. Barrow, Novel Microwave Microfluidic Sensor Using a Microstrip Split-Ring Resonator, *IEEE Trans. Microwave Theory Tech.*, 2014, **62**, 679–688.

51 P. M. Lambert and T. Polidore, 3D-Printed E-Band Gradient Dielectric Lens for Automotive and Industrial Applications, in *2022 IEEE International Symposium on Antennas and Propagation and USNC-URSI Radio Science Meeting (AP-S/URSI)*, IEEE, Denver, CO, USA, 2022, pp. 2074–2075, DOI: [10.1109/AP-S/USNC-URSI47032.2022.9886088](https://doi.org/10.1109/AP-S/USNC-URSI47032.2022.9886088).

52 J. O'Keefe, B. Roberts, B. Gray, K. Church and E. A. Rojas-Nastrucci, An Additively Manufactured CPW-back-fed Wideband Circularly-Polarized Radix Metasurface Patch Antenna for X-Band Space Applications, in *2023 IEEE International Conference on Wireless for Space and Extreme Environments (WiSEE)*, 2023, IEEE, Aveiro, Portugal, 2023, pp. 19–22, DOI: [10.1109/WiSEE58383.2023.10289327](https://doi.org/10.1109/WiSEE58383.2023.10289327).

